JOURNAL OF SPACECRAFT AND ROCKETS
Vol. 32, No. 5, September–October 1995

Numerical Investigation of Supersonic Vortical Flow About a Missile Body

J.-M. Moschetta*
Ecole Nationale Supérieure de l'Aéronautique et de l'Espace, 31400 Toulouse, France
A. Lafon†
Centre d'Etudes et de Recherches de Toulouse, 31400 Toulouse, France
and
H. Deniau‡
Aérospatiale Missiles, Verrières le Buisson, France

Three-dimensional supersonic viscous flow computations including crossflow separation are presented for an ogive–cylinder at an angle of attack varying from 0 to 20 deg. Solutions are obtained for the parabolized Navier–Stokes equations from an algorithm that incorporates a fully upwind implicit approach. Results are presented for laminar flow assumption and include side-by-side comparison with wind-tunnel data. Excellent agreement is obtained between computations and wind-tunnel measurements at $M_\infty = 2$ in terms of surface pressure distribution, body streamline pattern, and stagnation pressure contours in crossflow planes.

Nomenclature

A_l = attachment lines, $l = 1, 2 \ldots$
D = diameter of the cylinder, mm
$\hat{E}, \hat{F}, \hat{G}$ = flux vectors in curvilinear coordinates
J = metric Jacobian
L = body length, mm
M = Mach number
Re_D = Reynolds number based on D
T = static temperature, K
U = conservative state vector

Subscripts

i = inviscid flux
o = split pressure gradient
OC = Osher–Chakravarthy flux
v = viscous flux
∞ = freestream condition

Superscripts

$*$ = streamwise viscous derivatives neglected
I = first-order flux
II = second-order flux
N = numerical flux

Introduction

CURRENT applications of modern tactical missiles require increased aerodynamic performance and high maneuverability at supersonic speeds. If the angle of attack is sufficiently high to cause the formation of streamwise vortical structures on the leeside of the body, the problem of predicting the detailed flow characteristics near the missile is an important one for the preliminary designer, because the interaction of this leeside vortical flow with control surfaces, such as fins and tails, contributes to highly nonlinear aerodynamics. Euler solutions can account for the formation of vortices arising from smooth-body boundary-layer separation if some local treatment, such as a Kutta condition along the separation line, is applied. A boundary-layer code is necessary to provide the separation-line location, and a weak-coupling technique between the two methods has to be used.[1,2] However, great discrepancies between calculation and experimental data are observed on the location of the vortex cores, and the stagnation pressure loss in the vortices is generally underpredicted by Euler solvers. Because of their efficiency and ability to compute some of the complex phenomena involved in the aerodynamics exhibited by tactical missiles at angle of attack, the parabolized Navier–Stokes (PNS) equations are widely used in the design process. Solutions of these equations are obtained by marching in space rather than time and are therefore obtained much more efficiently than are solutions to the unsteady Navier–Stokes equations. The PNS equations contain all of the terms of both Euler and boundary-layer equations and consequently the interaction between the viscous and inviscid portions of the flowfield is automatically taken into account. Furthermore, as long as the streamwise component of the velocity remains positive, the PNS equations are still valid for crossflow separation around missile bodies. The present investigation is directed toward applying an extended version of the PNS code TORPEDO[3] to an ogive–cylinder configuration at $M_\infty = 2.0$, $Re_D = 1.61 \times 10^5$, and α varying from 0 to 20 deg. The flow conditions, chosen to correspond with the experimental case[4,5] are such that the flow is assumed to be laminar. This configuration was chosen because it provides a considerable number of measured data such as oil flow patterns, surface pressure distributions, and stagnation pressure distributions in different crossflow planes. The objectives of this study are 1) to validate the current approach by comparing computational results with wind-tunnel data and 2) to provide a detailed description of the flowfield and aerodynamics governing the flow at angle of attack.

Governing Equations

The three-dimensional steady PNS equations are written in a body-fitted coordinate system. They are expressed in a usual conservation-law form as

$$(\hat{E}_o)_\xi + \left(\hat{F}_i - \hat{F}_v^*\right)_\eta + \left(\hat{G}_i - \hat{G}_v^*\right)_\zeta = 0 \tag{1}$$

where ξ, η, ζ respectively denote the streamwise marching direction, the direction normal to the body, and the transverse direction. The subscripts i and v respectively identify the inviscid and the viscous terms, the circumflex ^ indicates scaling with respect to the Jacobian

---

Received June 28, 1994; revision received March 21, 1995; accepted for publication March 22, 1995.

*Associate Professor, Department of Aerodynamics; E-mail: moscheta@supaero.fr. Member AIAA.

†Research Scientist; current address: Direction des Recherches et Etudes Techniques, 00460 Armées, France. Member AIAA.

‡Ph.D. Student; currently at the Department of Aerothermodynamics, Centre d'Etudes et de Recherches de Toulouse, Toulouse 31400, France.

of the coordinate transformation, and the asterisk * on the normal and transverse viscous fluxes $\hat{F}_v$ and $\hat{G}_v$ denotes that streamwise viscous gradients are neglected. In order for Eq. (1) to be hyperbolic–parabolic in the streamwise marching direction, only a portion ω of the streamwise pressure gradient is retained, following the approach developed by Vigneron et al.,[6] which is indicated by the subscript o on the streamwise inviscid flux. The streamwise inviscid flux is then given by

$$\hat{E}_o = \begin{pmatrix} \rho\hat{U} \\ \rho u\hat{U} + \xi_x\omega p \\ \rho v\hat{U} + \xi_y\omega p \\ \rho w\hat{U} + \xi_z\omega p \\ (E+p)\hat{U} \end{pmatrix} \tag{2}$$

where

$$\hat{U} = \frac{\xi_x u + \xi_y v + \xi_z w}{J}, \qquad J = \frac{\partial(\xi,\eta,\zeta)}{\partial(x,y,z)} \tag{3}$$

$$\omega = \min\left(1, \sigma\frac{\gamma M_\xi^2}{1+(\gamma-1)M_\xi^2}\right) \tag{4}$$

M_ξ is the Mach number in the ξ-direction, and σ a safety factor included to provide for nonlinearities not accounted for in Vigneron's analysis. From Eq. (4), it appears that the streamwise pressure gradient treatment is only applied within the subsonic part of the flowfield. In the present case, in spite of the moderate value of the freestream Mach number, there are no regions outside the boundary layer where the Mach number is less than one. The system of equations is closed by the perfect-gas law and Sutherland's law for the viscosity coefficient.

Numerical Method

Using an implicit finite-volume formulation, discretization of the governing equation (1) results in

$$(\hat{E}_o)^{n+1}_{j,k} - (\hat{E}_o)^{n}_{j,k} + \left(\hat{F}_i - \hat{F}^*_v\right)^{n+1}_{j+\frac{1}{2},k} - \left(\hat{F}_i - \hat{F}^*_v\right)^{n+1}_{j-\frac{1}{2},k}$$

$$+ \left(\hat{G}_i - \hat{G}^*_v\right)^{n+1}_{j,k+\frac{1}{2}} - \left(\hat{G}_i - \hat{G}^*_v\right)^{n+1}_{j,k-\frac{1}{2}} = 0 \tag{5}$$

The associated linearized implicit form leads to the following block–pentadiagonal system of algebraic equations:

$$(\Lambda_0)^n\delta^{n+1}U_{j,k} + (\Lambda_1)^n\delta^{n+1}U_{j+1,k} + (\Lambda_2)^n\delta^{n+1}U_{j-1,k}$$

$$+ (\Lambda_3)^n\delta^{n+1}U_{j,k+1} + (\Lambda_4)^n\delta^{n+1}U_{j,k-1} = \mathrm{RHS}^n_{j,k}$$

$$\mathrm{RHS}^n_{j,k} = -\left[(\hat{A}_o)^{n+1} - (\hat{A}_o)^n\right]U^n - \left(\hat{F}_i - \hat{F}^*_v\right)^{n}_{j+\frac{1}{2},k}$$

$$+ \left(\hat{F}_i - \hat{F}^*_v\right)^{n}_{j-\frac{1}{2},k} - \left(\hat{G}_i - \hat{G}^*_v\right)^{n}_{j,k+\frac{1}{2}} + \left(\hat{G}_i - \hat{G}^*_v\right)^{n}_{j,k-\frac{1}{2}}$$

where the Λ_i are the Jacobian matrices resulting from the linearization of viscous and inviscid fluxes. The system of algebraic equations is solved using an efficient double ADI iterative method[3] that provides a converged solution of the full pentadiagonal system. The viscous fluxes are evaluated using conventional second-order accurate central differencing, and the inviscid fluxes $\hat{F}_i$ and $\hat{G}_i$ are discretized using high-order accurate non-MUSCL upwind schemes:

$$\hat{F}^N_{j+\frac{1}{2}} = \hat{F}^I_{j+\frac{1}{2}} + \hat{F}^{II}_{j+\frac{1}{2}} \tag{6}$$

where the numerical flux $\hat{F}$ is either $\hat{F}_i$ or $\hat{G}_i$. The numerical flux of Roe's first-order accurate upwind scheme is defined by

$$\hat{F}^{\mathrm{I}}_{j+\frac{1}{2}} = \tfrac{1}{2}\left[\hat{F}_j + \hat{F}_{j+1} - (\operatorname{sgn}\bar{D})_{j+\frac{1}{2}}(\hat{F}_{j+1} - \hat{F}_j)\right] \tag{7}$$

where the Jacobian matrix $\bar{D} = \partial F/\partial E$ is obtained from the solution of the linearized Riemann problem in each transverse direction. For the PNS equations, the linearized Riemann problem in the η direction is defined by

$$\frac{\partial\bar{E}_o}{\partial\xi} + \bar{D}_{j+\frac{1}{2}}\frac{\partial\bar{E}_o}{\partial\eta} = 0 \tag{8}$$

with initial conditions

$$\bar{E}_o = \begin{cases} \bar{E}_{oj}, & \eta \le \eta_{j+\frac{1}{2}} \\ \bar{E}_{oj+1}, & \eta > \eta_{j+\frac{1}{2}} \end{cases} \tag{9}$$

In the above approximate Riemann problem, $\bar{E}_o$ stands for $\hat{E}_o(U,\bar{\omega})$ and $\bar{\omega}$ is an approximate value of ω at the interface $j+1/2$. As suggested by Lafon et al.,[7] $\bar{\omega}$ may be defined as

$$\bar{\omega} = \min(\omega_j, \omega_{j+1}) \tag{10}$$

where ω_j is calculated from Eq. (4). In a previous version of the code, the upwind scheme was only applied in the supersonic region of the flowfield, and central differences were used within the subsonic part of the boundary layer as in Ref. 8. The above fully upwind technique turned out to be crucial to compute the flowfield at moderate Mach number, for which the previous switching strategy proved to be unstable. To upgrade the scheme's accuracy, a corrective term has been added to the above first-order upwind scheme, following Osher and Chakravarthy's approach.[9,10] The corrective flux is given by

$$\left(F^{\mathrm{II}}_{j+\frac{1}{2}}\right)_{\mathrm{OC}} = \frac{1-\Phi}{4}\left(\widetilde{\widetilde{\mathrm{d}F_1^+}}\right) + \frac{1+\Phi}{4}\left(\widetilde{\mathrm{d}F_2^+}\right)$$

$$-\frac{1+\Phi}{4}\left(\widetilde{\widetilde{\mathrm{d}F_2^-}}\right) - \frac{1-\Phi}{4}\left(\widetilde{\mathrm{d}F_3^-}\right) \tag{11}$$

where Φ is the upwinding parameter that defines schemes of varying accuracy, as can be seen by looking at the truncation error for the unlimited version of the schemes. In the present study, Φ has been taken equal to -1. The expressions for the flux differences $\mathrm{d}F$ can be found in Refs. 9 and 10 and are omitted here for brevity. The most dissipative value of the compression parameter $b = 1$ and the minmod slope limiter have been used in all our calculations.

Experimental Model and Test Conditions

Improvement and validation of the present PNS method require as complete as possible experimental descriptions of the flow around missile-type bodies at incidence. Although a certain number of experimental results are available for this type of flow,[11,12] only the experimental study of Pagan et al.[5] provides a complete data base including 1) detailed surface pressure distributions, 2) oil flow visualizations to determine separation lines, and 3) accurate flowfield measurements defining the vortex pattern. The model used for the experimental study was a nine-caliber ogive–cylinder body equipped with a three-caliber circular ogive of total length $L = 270$ mm and diameter $D = 30$ mm. It was sting-mounted so that its incidence α could be varied from 0 to 20 deg. The freestream conditions were

$$M_\infty = 2.0, \qquad Re_D = 1.61\times10^5, \qquad \gamma = 1.4$$

$$T_\infty = 183\,\mathrm{K}, \qquad Pr = 0.72$$

At these conditions, the flow was found to be laminar over the whole body. Therefore, only laminar computations are presented. However, computed results[13] for the turbulent regime have been recently obtained for the same flow conditions using the same code with algebraic and two-equation turbulence models.

Results and Discussion

The three-dimensional grid around the body consists of 1800 crossflow planes perpendicular to the body axis and at a distance of $\Delta x = 5.0\times10^{-3}D$ from each other. In each crossflow grid, 200 points are equally spaced circumferentially and 45 points are spaced exponentially from the body to a circular-shaped outer boundary.

Therefore, 16,200,000 grid points are used to represent the entire flowfield domain. The PNS solution for the whole body at each incidence required approximately 2 CPU hours on a Cray X-MP. This grid produced a constant normal cell size next to the wall of $5.0 \times 10^{-4} D$, which provided about 10 points in the boundary layer for $X/D = 8$. Boundary conditions are implicitly implemented through the specification of fluxes at the boundary faces. On the body surface, no-slip and isothermal wall conditions are imposed. At the inflow plane, uniform freestream conditions are imposed and a stepback technique is used to generate a conical solution around the apex of the body. Conditions at the far-field boundary are specified through the resolution of a local steady Riemann problem, canceling the reflection of pressure disturbances due to the bow shock. These nonreflecting far-field boundary conditions proved to allow a cylindrical outer boundary (Fig. 1) that minimizes grid distorsion and a better flowfield resolution in the vicinity of the body surface. Otherwise, at a low Mach number, such as 2.0 as in the present study, the computational domain would have had to be quite large in order to capture the bow shock. The flow is assumed to be symmetrical with respect to the pitch plane, so only half of the crossflow plane actually needs to be computed.

Surface Pressure Distribution

Lines of constant values of the reduced static pressure p/p_{t0} in the $(X/D, \varphi)$ plane are plotted in Figs. 2–5. The experimental primary separation line is also represented in these figures. In the experimental study, 17 pressure taps were equally distributed along a meridian line. The surface pressure distribution was obtained by rotating the model around its roll axis by an increment of 5 deg. This technique provided a total of 612 surface pressure values for one half of the body surface. Each figure compares computed results with measured data at the same incidence. Excellent agreement is obtained between computation and experiment for each incidence. Although computed isopressure contours are very close to the experimental data, the overall experimental pressure level is slightly higher than calculations for all values of the angle of attack. Although at $\alpha = 5$ deg (Fig. 2) only streamwise pressure gradients are visible on the forebody ($X/D \leq 3$), transverse pressure gradients and a plateau of almost constant pressure can be observed at higher incidence (Figs. 4 and 5). The primary separation line typically divides the region of high pressure gradients from a relatively low-pressure plateau. This plateau is induced by the presence of a vortex. For $\alpha = 5$ deg, as noticed in the experimental analysis, separation does not produce an intense vortex as it does at higher incidences. Consequently, the pressure plateau is not clearly visible at $\alpha = 5$ deg.

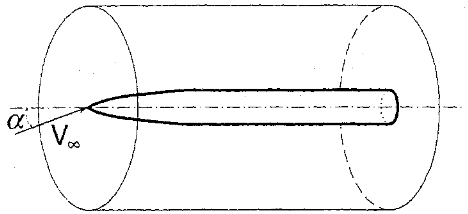

Fig. 1 Sketch of the computational domain for the ogive–cylinder geometry.

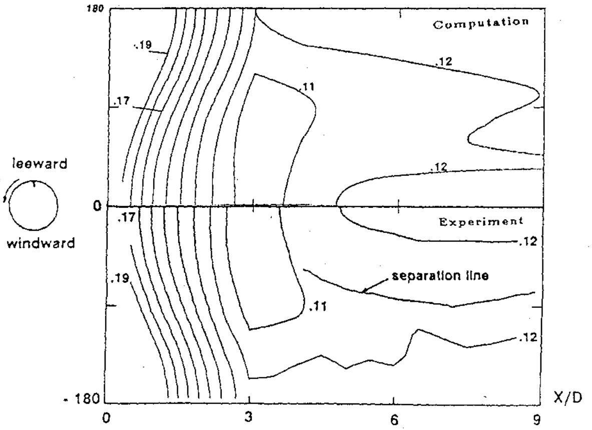

Fig. 2 Surface pressure distribution at $\alpha = 5$ deg.

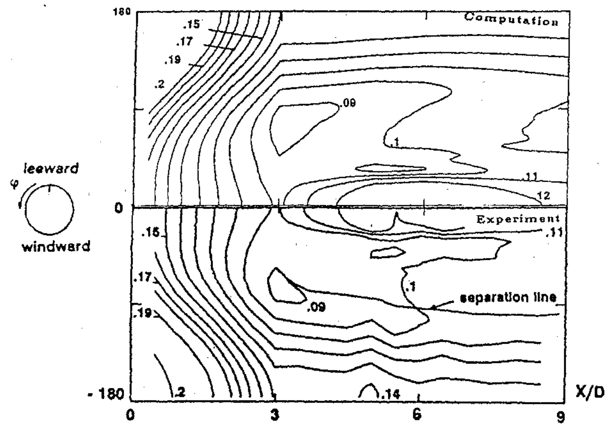

Fig. 3 Surface pressure distribution at $\alpha = 10$ deg.

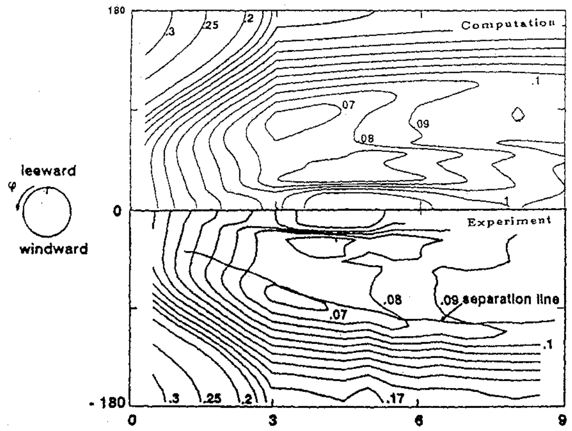

Fig. 4 Surface pressure distribution at $\alpha = 15$ deg.

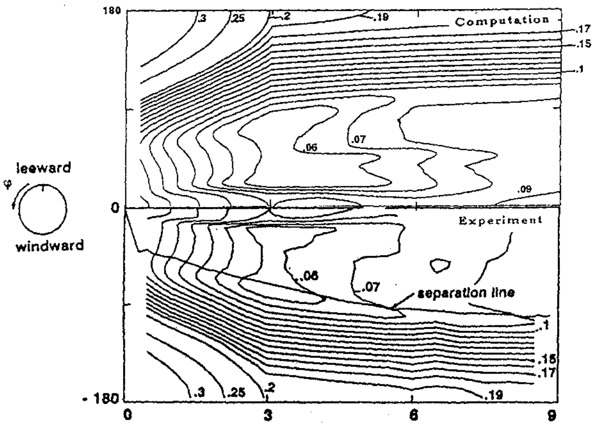

Fig. 5 Surface pressure distribution at $\alpha = 20$ deg.

Topological Analysis of Vortical Structures

Skin-friction line patterns in the $(X/D, \varphi)$ plane are presented in Figs. 6–13 with the corresponding transverse streamlines for $X/D = 8$. The primary separation line is also represented in these figures. As reported by Pagan et al.,[5] skin-friction line patterns are topologically equivalent for $\alpha = 5$ and 10 deg. Two attachment lines A_1 and A_2 are present respectively in the windward and the leeward symmetry plane. Primary separation occurs along line S_1, and skin-friction lines also converge toward a secondary separation line S_2. Between S_1 and S_2 a third attachment line A_3 is clearly visible on the computed results, whereas it was barely visible in the experimental oil flow visualizations.[5] For higher angles of attack ($\alpha = 15$ and 20 deg, Figs. 10–13), the singular lines A_1, A_2, A_3, S_1, and S_2 are

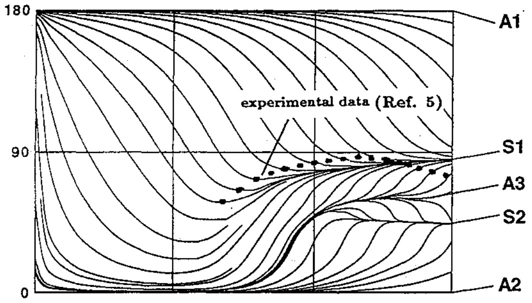

Fig. 6 Computed skin-friction pattern at α = 5 deg.

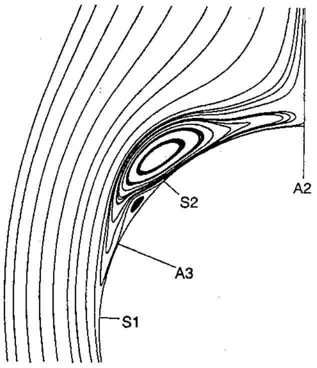

Fig. 7 Computed crossflow streamlines at α = 5 deg.

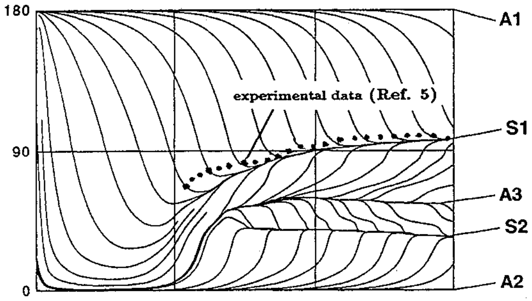

Fig. 8 Computed skin-friction pattern at α = 10 deg.

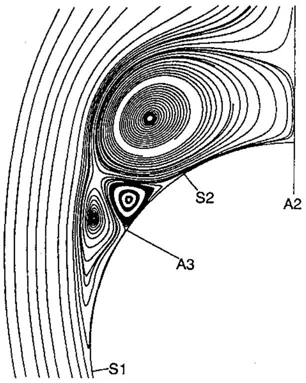

Fig. 9 Computed crossflow streamlines at α = 10 deg.

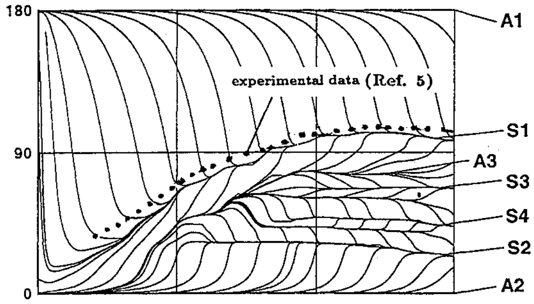

Fig. 10 Computed skin-friction pattern at α = 15 deg.

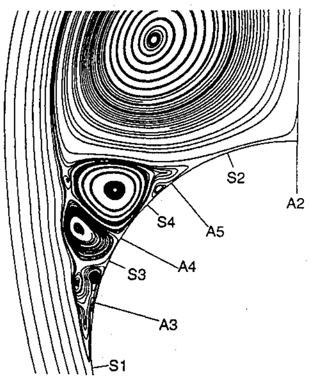

Fig. 11 Computed crossflow streamlines at α = 15 deg.

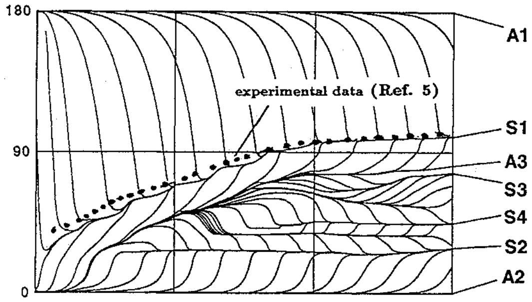

Fig. 12 Computed skin-friction pattern at α = 20 deg.

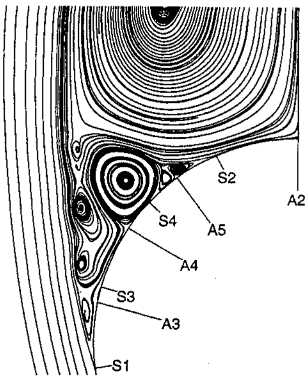

Fig. 13 Computed crossflow streamlines at α = 20 deg.

still present. In addition, between S_2 and A_3, two other separation lines S_3 and S_4 are clearly visible on the computational results. Their existence has been confirmed in the experimental observation.[5] As a consequence, in the crossflow plane, at least six vortices are visible, and their existence is fully consistent with analysis of the skin-friction line pattern. The topological analysis of crossflow vortical flows is based on critical-point theory[14] and is used here to confirm numerical findings. Topological laws specify relationships between the number of nodes (N) or half nodes (N') and the number of saddle points (S) or half saddles (S') present in the crossflow field (on both sides). As reported in Ref. 15, for streamlines on a two-dimensional plane cutting a three-dimensional body, the relevant topological law states that

$$(\Sigma N + \Sigma N'/2) - (\Sigma S + \Sigma S'/2) = -1 \tag{12}$$

Figure 14 shows the topological interpretation of the flow structure in a crossflow plane for α = 5 and 10 deg (Fig. 14a), for which the flow topology in the two cases is equivalent, and for α = 15 and 20 deg (Fig. 14b), for which the flow topology is also very similar. At 5 and 10 deg, the computed flowfield is fully consistent with the observations of Pagan et al.[5] In Fig. 14a, eight half saddle points corresponding to separation and attachment lines are visible on the body; six spiral nodes (N_1, N_2, N_3) and three saddle points by (S) can also be identified. Therefore, Eq. (12) is satisfied. At 15- and 20-deg angle of attack (Fig. 14b), the flowfield takes a much more complex form, consisting of several very small vortices not observed experimentally in Ref. 5. Including the primary and secondary

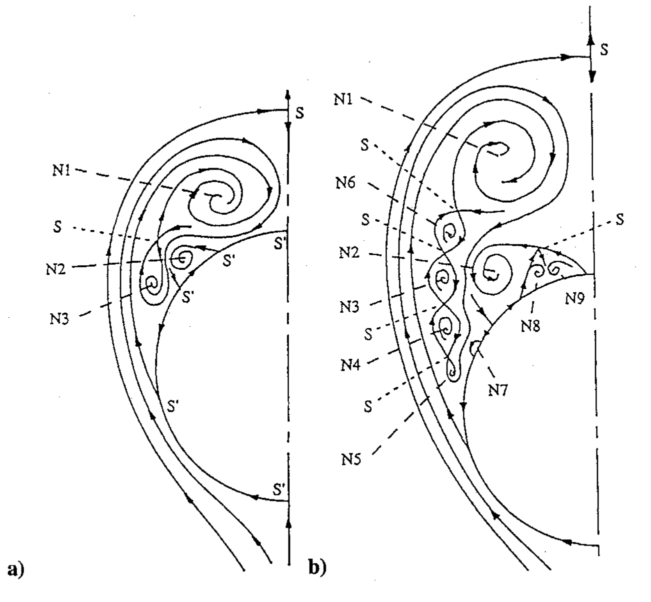

Fig. 14 Crossflow topological interpretation for a) $\alpha = 10$ deg and b) $\alpha = 20$ deg.

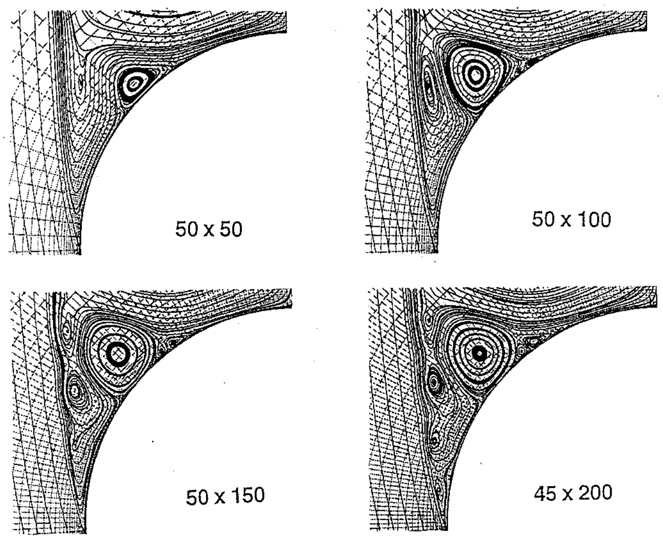

Fig. 15 Effect of grid refinement on the computed vortical structure at $\alpha = 20$ deg and $X/D = 8$.

vortices, the nodes identified in Fig. 14b sum to 18. There are 11 saddle points in the flowfield and 16 half saddle points on the body surface, which are omitted from the figure for clarity. Equation (12) applies in this case as well.

Mesh Sensitivity Analysis

A comparison of the computed crossflow streamlines for different grids has been made. Figure 15 shows the effect of transverse grid refinement only on the PNS solutions using four different grids: 50 × 50, 50 × 100, 50 × 150, and 45 × 200. Both streamwise and normal resolution are maintained constant, except for the last case (45 × 200) because of the memory limitation encountered. Comparison between the different grids indicates that transverse gradient resolution is of major importance for this kind of flow. The coarse grid (50 × 50) provides a small secondary vortex and a tiny third vortex, and a more refined grid (50 × 100) obtained by doubling the resolution in the transverse direction yields a larger secondary vortex. The shape and location of the secondary vortex hardly change when the grid is further refined in the transverse direction (50 × 150 or 45 × 200). A similar observation can be made for the third vortex that appears between the secondary vortex and the primary separation line: its shape and location are only slightly affected by refining the grid from 50 × 150 to 45 × 200. An equivalent refinement study has been made in the normal direction, keeping constant the resolution in the transverse direction. No noticeable changes could be observed in the crossflow topology on increasing the number of points in the normal direction. This mesh sensitivity study did not include a refinement in the longitudinal direction, since, because of stability requirements on the marching space step, 1800 points had to be distributed in the streamwise direction.

Crossflow Stagnation Pressure Distribution

The loss in total pressure sustained by the body vortices may affect the efficiency of downstream air-breathing missiles intakes. Therefore, the prediction of stagnation pressure levels in the flowfield is important for correctly designing and integrating air intakes on missile bodies. Side-by-side comparisons between computation and wind-tunnel measurements are presented in Figs. 16–19 in terms of stagnation pressure contours $p_{\mathrm{st}}/p_{\mathrm{st}0}$ for $\alpha = 20$ deg. For each crossflow plane ($X/D = 3, 5, 6, 8$), the experimental main vortex core location is accurately predicted and the numerical prediction for the total pressure loss at the vortex core is in close agreement with measured Pitot pressure. It can be observed that the stagnation pressure level at the center of the primary vortex is close to $p_{\mathrm{st}}/p_{\mathrm{st}0} = 0.25$–$0.3$ for each crossflow plane, which is adequately predicted by

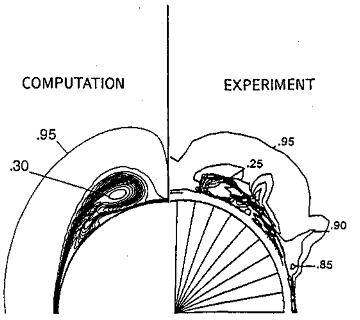

Fig. 16 Computed and experimental stagnation pressure contours for $X/D = 3$ at $\alpha = 20$ deg.

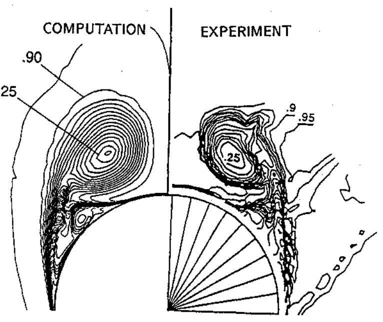

Fig. 17 Computed and experimental stagnation pressure contours for $X/D = 5$ at $\alpha = 20$ deg.

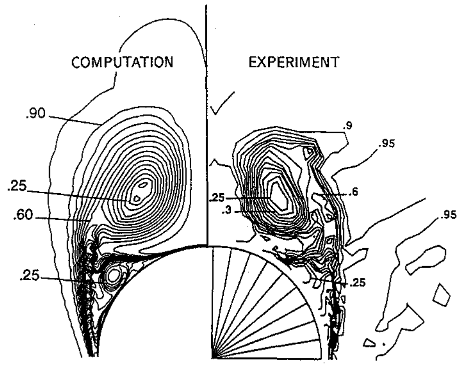

Fig. 18 Computed and experimental stagnation pressure contours for $X/D = 6$ at $\alpha = 20$ deg.

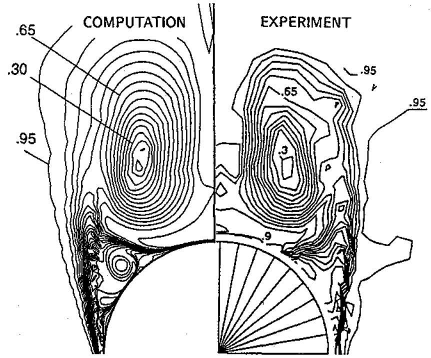

Fig. 19 Computed and experimental stagnation pressure contours for $X/D = 8$ at $\alpha = 20$ deg.

the computation. It appears clearly from Figs. 17–19 that the topology of the vortical structure is not changed along the cylindrical part of the body ($X/D = 3$ to 8) even though the whole structure tends to become larger downstream. The separated vortex sheet, which rolls up to constitute the primary vortex, is a region characterized by low values of stagnation pressure ($p_{st}/p_{st0} = 0.25$). Surprisingly, almost the same value of the stagnation pressure ($p_{st}/p_{st0} = 0.25$) is obtained for the secondary vortex regardless of the differences with the primary vortex in terms of size and intensity (see for example Fig. 18). It is also noteworthy that the stagnation pressure level at the center of the primary and the secondary vortices remains almost constant along the body (compare Figs. 16 and 19). This suggests that most of the stagnation pressure loss in the vortical crossflow structure is due to the viscous dissipation when the fluid particles that are going to separate are still inside the boundary layer. Consequently, this stagnation pressure loss results only for a small part from the rolling-up movement of the vortex sheet in the flowfield.

Conclusion

An extensive numerical study of the supersonic crossflow separation around an ogive–cylinder at incidence has been presented. Detailed side-by-side comparisons between measured data and computed results have been analyzed to correctly predict and understand the complex flow structure of laminar crossflow separation in the supersonic regime. Close agreement obtained between computational and experimental results on the surface pressure distribution, skin-friction line pattern, crossflow topology, and total pressure contours, is a strong indication of the accuracy of the present fully upwind PNS method for this kind of flow. Both experimental and computed results have been used to provide a detailed understanding and a reliable topological interpretation of the three-dimensional separation phenomenon.

References

[1] Lordon, J., Fare, J.-C., and Pagan, D., "Supersonic Vortex Flows Around a Missile Body—Basic Experiment and Euler Numerical Computation," AGARD Rept. CP-493, Oct. 1990, pp. 15.1–15.7.

[2] Priolo, F. J., and Wardlaw, A. B., "Euler-Space Marching Computations with Crossflow Separation for Missile-Type Bodies," AIAA Paper 90-0616, Jan. 1990.

[3] Moschetta, J.-M., "Calculs d'Écoulements Supersoniques Turbulents par Résolution des Équations de Navier–Stokes Parabolisées," Ph.D. Thesis, CERFACS/Inst. National Polytechnique de Toulouse, Toulouse, Nov. 1991; CERFACS Rept. TH/RF/91/8.

[4] Pagan, D., and Molton, P., "Etude Expérimentale du Système Tourbillonnaire Engendré par un Fuselage de Missile en Incidence," ONERA Rapport Technique 40/1147 AY, Jan. 1990.

[5] Pagan, D., Molton, P., and Délery J., "Basic Experiment on a Supersonic Vortex Flow Around a Missile Body," *Journal of Spacecraft and Rockets*, Vol. 29, No. 3, 1990, pp. 373–378.

[6] Vigneron, Y. C., Rakich J. V., and Tannehill, J. C., "Calculation of Supersonic Viscous Flow over Delta Wings with Sharp Subsonic Leading Edges," NASA TM-78500, AIAA Paper 78-1137, July 1978.

[7] Lafon, A., Deniau, H., Maman, P., and Moschetta, J.-M., "A Fully Upwind Implicit PNS Solver for the Computation of 3D Supersonic Flows with Crossflow Separation," AIAA Paper 94-0643, Jan. 1994.

[8] Lawrence, S. L., "Upwind Algorithm for the Parabolized Navier–Stokes Equations," *AIAA Journal*, Vol. 27, No. 9, 1989, pp. 1175–1183.

[9] Chakravarthy, S. R., Szema, K.-Y., Goldberg, U. C., Gorsky, J. J., and Osher, S., "Application of a New Class of High Accuracy TVD Schemes to the Navier–Stokes Equations," AIAA Paper 85-0165, Jan. 1985.

[10] Chakravarthy, S. R., and Osher, S., "A New Class of High Accuracy TVD Schemes for Hyperbolic Conservation Laws," AIAA Paper 85-0363, Jan. 1985.

[11] Champigny, P., and Baudin, D., "Ecoulement Tourbillonnaire sur Fuselage de Missile, Etude Expérimentale et Modélisation," AGARD Rept. CP-494, July 1991, pp. 17.1–17.9.

[12] Ragsdale, W. C., "Flow Field Measurement Around an Ogive–Cylinder at Angle of Attack up to 15 Degrees for Mach Number of 3.5 and 4.0," Naval Ordonance Lab., TR 72-198, Silver Spring, MD, Aug. 1972.

[13] Deniau, H., Lafon, A., and Moschetta, J.-M., "Progress in the Development and Validation of a Turbulence Model for the Computation of 3D Supersonic Flows with Crossflow Separation," AIAA Paper 95-0090, Jan. 1995.

[14] Visbal, M. R., and Gordnier, R. E., "Crossflow Topology of Vortical Flows," *AIAA Journal*, Vol. 32, No. 5, 1994, pp. 1085–1087.

[15] Shen, G., and Philpott, D., "The Application of Topology to the Interpretation of Cross Flows and Some New Extensions," AIAA Paper 89-0568, Jan. 1989.

K. J. Weilmuenster
Associate Editor